How do atmospheric rivers form?

Article

Published Version

Dacre, H. F. ORCID: https://orcid.org/0000-0003-4328-9126, Clark, P. A. ORCID: https://orcid.org/0000-0003-1001-9226, Martinez-Alvarado, O. ORCID: https://orcid.org/0000-0002-5285-0379, Stringer, M. A. and Lavers, D. A. (2014) How do atmospheric rivers form? Bulletin of the American Meteorological Society, 96 (8). pp. 1243-1255. ISSN 1520-0477 doi: 10.1175/BAMS-D-14-00031.1 Available at https://centaur.reading.ac.uk/38124/

SPECIAL
DIAMET
COLLECTION

HOW DO ATMOSPHERIC RIVERS FORM?

BY H. F. DACRE, P. A. CLARK, O. MARTINEZ-ALVARADO, M. A. STRINGER, AND D. A. LAVERS

Identifying the source of atmospheric rivers: Are they rivers of moisture exported from the subtropics or footprints left behind by poleward traveling storms?

Studies of heavy precipitation occurring in the winter over land in the midlatitudes have found that these events are almost always associated with extratropical cyclones (Lackmann and Gyakum 1999; Viale and Nunez 2011; Hawcroft et al. 2012). These heavy precipitation events often occur when warm moist air, located in the cyclone's warm sector, encounters orography (e.g., along the west coast of the United States or United Kingdom), resulting in significant precipitation enhancement (Hand et al. 2004; Ralph et al. 2004; Neiman et al. 2008). These events involve a combination of large-scale synoptic and mesoscale processes in an orographic precipitation-enhancement mechanism known as the seeder–feeder mechanism (Bader and Roach 1977). In this process, precipitation from the cyclone's upper-level cloud features (seeder clouds) falls through a lower-level mesoscale orographic stratus cloud (feeder cloud) capping a hill or small mountain and thus producing greater precipitation on the hill under the cap cloud than on the nearby flat land. While this mechanism does not change the total cyclone associated precipitation greatly, it can act to redistribute the precipitation and concentrate it over regions of orography. The effectiveness of the process depends on sufficiently strong low-level moist flow to maintain the cloud water content in the orographic feeder cloud and the continuing availability of precipitation from the seeder cloud (Hill et al. 1981; Browning 1990). In particular, moist air masses at levels below 1 km have been found to be critical to the moisture convergence associated with orographic precipitation enhancement in the coastal mountains of the western United States and United Kingdom (Smith et al. 2010; Neiman et al. 2011).

One common method for identifying these warm, moist low-level air masses is to detect filaments of high total column water vapor (TCWV) extending from the subtropics using satellite data. These 2D filamentary structures suggest long-distance, riverlike moisture transport and are routinely used as a proxy for identifying regions of strong water vapor transport (atmospheric rivers). High TCWV and strong low-level winds in the pre–cold frontal region lead to intense poleward moisture transport (Ralph et al. 2004, 2013) and have been associated with flooding in the United States and United Kingdom (Lavers et al.

AFFILIATIONS: DACRE, CLARK, MARTINEZ-ALVARADO, AND STRINGER—Department of Meteorology, University of Reading, Reading, United Kingdom; LAVERS—Iowa Institute of Hydraulic Research–Hydroscience and Engineering, The University of Iowa, Iowa City, Iowa
CORRESPONDING AUTHOR: Helen Dacre, Department of Meteorology, University of Reading, Earley Gate, P.O. Box 243, Reading RG6 6BB, United Kingdom
E-mail: h.f.dacre@reading.ac.uk

The abstract for this article can be found in this issue, following the table of contents.
DOI:10.1175/BAMS-D-14-00031.1

In final form 31 October 2014

2011; Neiman et al. 2011; Ralph et al. 2013; Lavers et al. 2012). Trajectory case studies, however, have shown that atmospheric rivers do not represent true trajectories of water vapor transport (Bao et al. 2006). Rather, they depict the instantaneous position of corridors of enhanced water vapor in the portion of an extratropical cyclone known as the warm conveyor belt (Harrold 1973), which occurs near the leading edge of the cold front.

In a 23-year climatology of tropical moisture export, Knippertz and Wernli (2010) showed that trajectories that start south of 35°N largely recirculate toward the low latitudes before reaching the extratropics. Thus, while long-range transport of moisture from southerly latitudes can increase during atmospheric river events, the majority of precipitation in the extratropics is due to moisture evaporating at local or nearby latitudes (Sodemann and Stohl 2013). Any tropical moisture transport that does reach the extratropics appears to occur above the boundary layer and thus contributes to midlevel moisture (Knippertz and Martin 2007; Sodemann and Stohl 2013). Thus, although high TCWV bands appear to move and extend eastward in satellite animations, their leading ends are actually the manifestation of moisture convergence associated with warm conveyor belts that move with the extratropical cyclone (Bao et al. 2006; Cordeira et al. 2013).

To further elucidate the physical processes responsible for high TCWV band formation, Boutle et al. (2010) performed idealized modeling of an extratropical cyclone. They found that moisture is evaporated from the sea surface and transported large distances within the boundary layer toward the base of the warm conveyor belt airflow. Horizontal divergence forced by boundary layer drag and large-scale ageostrophic flow transports moisture away from these regions, which maintains the saturation deficit, allowing strong evaporation to be maintained. This is a continual process occurring throughout the life cycle, ensuring that the base of the warm conveyor belt airflow always contains moisture (Boutle et al. 2011). Thus, rather than consuming water vapor in preexisting high TCWV bands, as suggested by Zhu and Newell (1998), individual cyclones contribute to the formation and maintenance of high TCWV bands at the leading end by adding moisture accumulated ahead of their cold fronts (Bao et al. 2006; Sodemann and Stohl 2013).

Despite this, much published work on atmospheric rivers continues to assert that atmospheric rivers achieve their high water vapor content through direct transport from the tropics (e.g., Rivera et al. 2014; Rutz et al. 2014; Neiman et al. 2013; Wick et al. 2013; Dettinger 2013; Matrosov 2013; Guan et al. 2013; Kim et al. 2013; Moore et al. 2012). In this paper, we aim to illustrate the intrinsic role that extratropical cyclones have in atmospheric river formation. The misconception that moisture filaments are drawn into developing cyclonic circulations and that atmospheric rivers deliver large masses of warm, moist air directly from the tropics to the extratropics are addressed. Finally, use of the term "atmospheric river" as a suitable descriptor of these moist airflows is discussed.

In this paper, we will perform a kinematic analysis of the properties of a climatology of 200 extratropical cyclones and quantify the relative contribution of different processes leading to the formation of high TCWV bands in the atmosphere. This is achieved by calculating the water vapor budget for each cyclone in a frame of reference that moves with the cyclone. This allows us to determine how processes leading to the formation of atmospheric rivers evolve as the cyclone develops. Furthermore, tracking the cyclones relative to their time of maximum intensity allows us to composite the water vapor budget for a whole climatology of cyclones and thus generalize our results beyond individual case studies. This analysis quantifies in reanalysis data the role played by different aspects of the flow within extratropical cyclones in generating the features commonly identified as atmospheric rivers. It does not attempt to explain the dynamics of extratropical cyclones that generate the flows we have analyzed. For example, we consider the contribution of the horizontal convergence of the wind to the overall moisture convergence; this is equivalent to the role of vertical motion, which both generates and is enhanced by latent heating associated with cloud processes. Such feedback-driven enhancement is included in our analysis but is not isolated as a separate factor.

METHOD. *Cyclone tracking and dataset.* Following the work of Catto et al. (2010), we apply an objective cyclone identification and tracking algorithm (Hodges 1995) to fields from the Interim European Centre for Medium-Range Weather Forecasts (ECMWF) Re-Analysis (ERA-Interim) for the winter periods (December–February) of 1989–2009 (Dee et al. 2011). The temporal resolution of the data is 6 hourly. Tracks are identified using the 850-hPa relative vorticity truncated to T42 resolution (approximately 2.8°) to emphasize the synoptic scales. The 850-hPa relative vorticity features have been filtered to remove stationary cyclones (traveling <1000 km during their lifetimes) or short-lived cyclones (lifetimes < 48 h). Evaluation of the tracking algorithm, for a subset of the individual cyclones studied in this paper using high-resolution satellite data, can be found on the Extratropical

Cyclone Atlas (www.met.rdg.ac.uk/~storms). Dacre et al. (2012) (their Fig. 1) show the 200 most intense, in terms of the T42 vorticity, winter cyclone tracks with maximum intensity in the North Atlantic (70°–10°W, 30°–90°N), which are used in this paper. The tracks have significant poleward motion with an average meridional displacement of 20.3°N. The required fields are extracted from the ERA-Interim dataset along the tracks of the selected cyclones within a 1500-km radius surrounding the identified cyclone position on constant pressure surfaces.

Water vapor budget. To determine the relative importance of processes leading to the formation of high TCWV bands in the atmosphere, we calculate the individual terms in the water vapor budget for each gridbox column within the cyclone system (defined here as a region within 1500 km of the cyclone center). The cyclone center is defined as the location of the maximum 850-hPa relative vorticity value. The water vapor budget in a column of air is given by

$$P - E = -\frac{1}{g}\int_{p_{500}}^{p_s} \frac{\partial q}{\partial t} dp - \frac{1}{g}\int_{p_{500}}^{p_s} \nabla \cdot (q\underline{u}) dp, \qquad (1)$$

where P is the surface precipitation flux (kg m^{-2} s^{-1}), E is the surface evaporation flux (kg m^{-2} s^{-1}), g is the acceleration due to gravity (m s^{-2}), q is the specific humidity (kg kg^{-1}), t is time (s), and $\underline{u}$ is the horizontal wind vector (m s^{-1}). Terms on the right-hand side of the equation are integrated from the surface to 500 hPa as water vapor transport above 500 hPa is found to contribute only a small amount (~1%) to the gridbox total, reflecting the decrease in specific humidity with height. Accumulated precipitation (P) and evaporation (E) are not available as analyzed fields in ERA-Interim and are therefore taken from short-range forecast accumulations. The ERA-Interim forecast estimates have previously been found to compare well to gridded gauge data (Simmons et al. 2010) and to the Global Precipitation Climatology Project (GPCP) combined satellite and rain gauge product (Hawcroft et al. 2012). During the first hours of the forecast simulation, the precipitation field is affected by spinup. Given the requirement to have 6-hourly accumulations centered on 0000, 0600, 1200, and 1800 UTC, the forecast periods utilized in this study are accumulations from 9 to 15 h and from 15 to 21 h for forecasts starting at 1200 UTC the previous day and from 9 to 15 h and from 15 to 21 h for forecasts starting at 0000 UTC the same day. Recent work indicates that the lead time used in this paper offers the best estimates available from ERA-Interim given the 6-hourly accumulations required for this study (de Leeuw et al. 2015). All other fields are analyzed as described in Dee et al. (2011).

The first term on the right-hand side of Eq. (1) represents the vertically integrated rate of change of water vapor in the column dq/dt. The second term on the right-hand side of Eq. (1) represents the vertically integrated divergence of water vapor from the column. Usually the negative of the second term is used and commonly referred to as the moisture flux convergence (MFC_{TOT}). The moisture flux convergence term in Eq. (1) can be split into two parts,

$$-\frac{1}{g}\int_{p_{500}}^{p_s} \nabla\cdot(q\underline{u}) dp = -\frac{1}{g}\int_{p_{500}}^{p_s} \underline{u}\cdot\nabla q\, dp - \frac{1}{g}\int_{p_{500}}^{p_s} q\nabla\cdot\underline{u}\, dp. \qquad (2)$$

The first term on the right-hand side of Eq. (2) represents the vertically integrated horizontal advection of water vapor (MFC_{ADV}), and the second term represents the vertically integrated water vapor–weighted mass convergence (MFC_{CONV}). This term, of course, could also be written in terms of the water vapor–weighted vertical mass flux. In this paper, we will refer to these terms as the advection and mass convergence terms.

CASE STUDY: 1 FEBRUARY 2002. *Synoptic evolution.* To demonstrate the processes leading to the spatial distribution and transport of water vapor in extratropical cyclones, we first present the results for an example cyclone that caused flooding in the United Kingdom on 1 February 2002.

Figure 1 shows the track of an intense extratropical cyclone as it traveled northeastward from its genesis location in the North Atlantic to its lysis location in the Barents Sea. As it passed to the west of the United Kingdom, heavy precipitation associated with the cyclone between 0600 and 1200 UTC 1 February 2002 led to flooding in south Wales and Cumbria (regions of orography on the west coast of the United Kingdom). During this period, the cyclone was in its developing stage, reaching its highest 850-hPa vorticity value just south of Iceland.

Figure 2a shows the European Organisation for the Exploitation of Meteorological Satellites (EUMETSAT) infrared satellite image of the cyclone at 0600 UTC 1 February 2002 (−12 h on cyclone track; Fig. 1). At this point in the cyclone's evolution, the cloud structure has developed into a spiral-shaped pattern, with high-level cold cloud (bright white on image) wrapping cyclonically around the low pressure minima at the center of the figure (933 hPa; Fig. 2b).

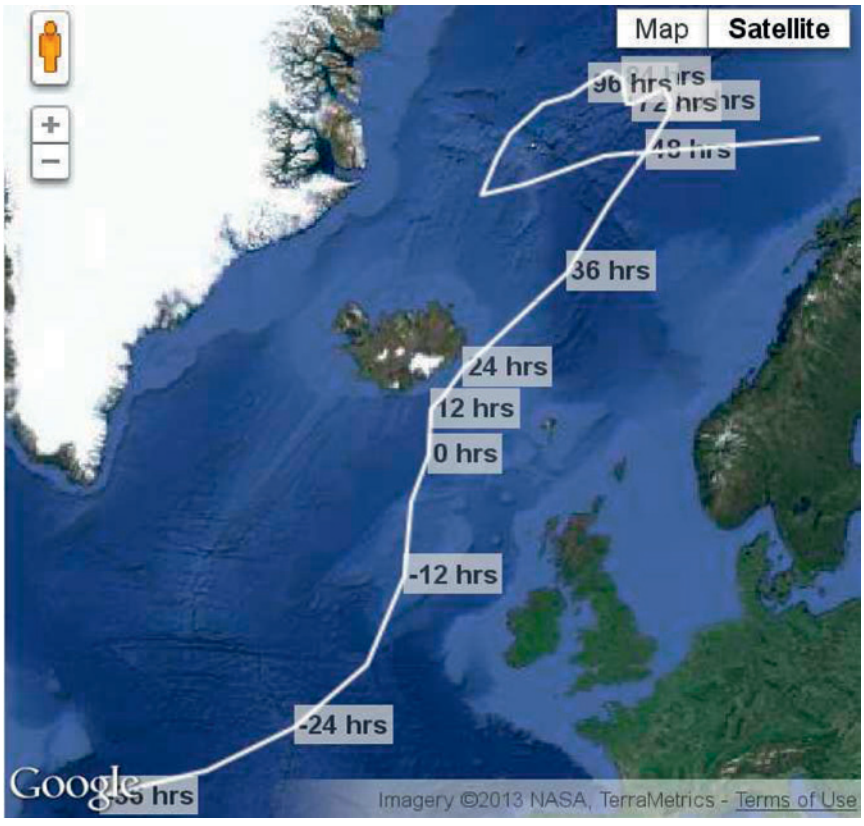

Fig. 1. Track of a cyclone that passed to the west of the United Kingdom between 0600 UTC 31 Jan and 0600 UTC 4 Feb 2002. Gray labels show the location of the cyclone at 12-hourly intervals, relative to its time of maximum 850-hPa relative vorticity (0 h). Image is from the Extratropical Cyclone Atlas (www.met.rdg.ac.uk/~storms).

The cloud head is positioned along the boundary of two air masses, as represented by the occluded front in Fig. 2b, and the polar front cloud band is observed positioned parallel to the surface cold front. Scattered convective cloud can be seen in the air behind the cold front, where cold air is advected over a relatively warm sea surface resulting in convective instability.

Beneath these cloud features are regions of precipitation. Figure 2c shows the ERA-Interim forecast 6-hourly accumulated precipitation at the surface (centered at 0600 UTC 1 February 2002). The precipitation pattern shows a similar spiral shape to the cloud features. Over this time the heaviest precipitation [>6 mm $(6\ h)^{-1}$] is located beneath the cloud head along the occluded front.

TCWV is a measure of the total amount of water vapor in the atmosphere. Figure 2d shows the instantaneous ERA-Interim TCWV. The highest values of TCWV are found in the cyclone's warm sector (bounded by the warm and cold fronts). A region of heavy precipitation beneath the polar front cloud band at the southernmost end of the cold front is found within the region of high TCWV air. Another region of heavy precipitation occurs along the occluded front close to the center of the cyclone and outside the region of high TCWV air. Thus, high TCWV is not a sufficient condition for heavy precipitation to occur. A column of air may have large absolute values of TCWV but not be saturated since higher temperature implies higher saturation vapor pressure. (The Clausius–Clapeyron equation, which determines the water-holding capacity of the atmosphere, predicts an increase of 7% for every 1°C rise in temperature.)

Figure 2e shows the instantaneous column-integrated saturation, calculated using ERA-Interim TCWV and temperature fields. High values of column saturation (>60%) are not restricted to the warm sector but extend across the warm frontal boundary, wrapping around the cyclone center. The column-integrated saturation shows a close correspondence with the cloud field pattern (Fig. 2a). Figure 2f shows the 500–300-hPa divergence field overlaid with 300-hPa wind speed isotachs. These fields give an indication of the large-scale environment in which the cyclone is developing. The cyclone is located in the left exit region of an upper-level jet, a favorable location for cyclogenesis, beneath a region of strong upper-level divergence.

Spatial distribution and magnitude of precipitation. In this section the spatial distribution and magnitude of precipitation and integrated water vapor transport (IVT) during the intensifying stage of the cyclone evolution is described. Figures 3a–c show the 6-hourly accumulated precipitation at three times during the development stage of the cyclone's evolution. Also shown in Figs. 3a–c are the positions of the surface cold, warm, and occluded fronts, plus the approximate location of the United Kingdom. The cyclone leading to precipitation and flooding in the United Kingdom

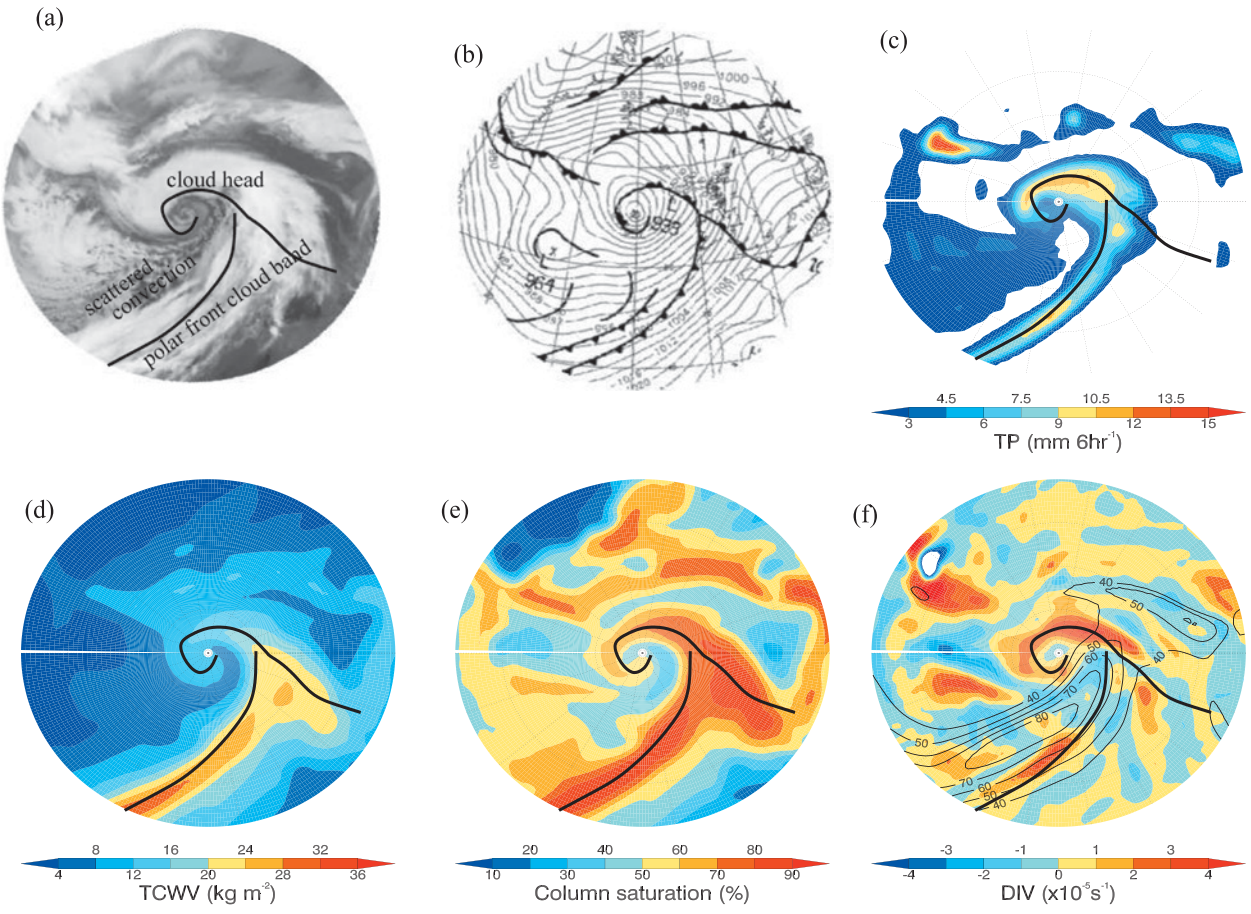

Fig. 2. Cyclone-centered fields at 0600 UTC 1 Feb 2002. (a) Infrared satellite image from EUMETSAT (available from www.met.rdg.ac.uk/~storms). (b) Met Office synoptic analysis chart. (c) Total precipitation [mm (6 h)$^{-1}$]. (d) Total column water vapor (kg m^{-2}). (e) The 1000–300-hPa column-integrated saturation (%) and (f) 500–300-hPa divergence ×10^{-5} s^{-1} overlaid with 300-hPa wind speed (m s^{-1}). All figures are overlaid with surface frontal positions.

on 1 February 2002 is a secondary cyclone (labeled "2") forming on the trailing cold front of a preexisting primary cyclone (labeled "1"). Cyclone 2 is located in the eastern North Atlantic 24 h before maximum intensity. Cyclones with genesis in the east Atlantic are often rapidly developing secondary cyclones, with a strong diabatic component (Gray and Dacre 2006; Dacre and Gray 2009, 2013). Cyclone 1 is in its mature stage of development and is beginning to dissipate (as described in the 1 February 2002 case study section above). Both cyclones 1 and 2 are associated with high IVT values located ahead of and parallel to the respective cyclone's cold front (Fig. 3d). The 250 kg m^{-1} s^{-1} IVT contour is shown for comparison with papers such as Rutz et al. (2014), which uses this threshold to define atmospheric rivers. In this paper, we have not used this threshold to delineate atmospheric rivers since, for this case study, the threshold identifies a region that encompasses both the narrow band of high IVT and the broader warm conveyor belt region, and as such the atmospheric river is not a subset of the warm conveyor belt (as suggested in the literature) but a much broader region. Figure 3b shows cyclone 2's location 12 h later. It is now located closer to the United Kingdom and is more wrapped up, with a longer occluded front and a narrower warm sector. Again, high IVT values are found in the cyclone's warm sector (Fig. 3e). However, it should be noted that while high domain averaged IVT is correlated with high precipitation totals (Ralph et al. 2013) the location of the heavy precipitation does not always coincide with the high IVT locations. The heaviest precipitation is often found on the occluded front beneath the cloud head in a region where IVT is low. Finally, Fig. 3c shows the location of cyclone 2 a further 12 h later, at the time of maximum intensity. By this time, the cyclone has traveled to the north of the United Kingdom and the precipitation along the occluded front is becoming less coherent. IVT in the warm sector has also been reduced (Fig. 3e). A third cyclone (labeled "3") is forming on the trailing cold front of cyclone 2 and is tracking along the same path as cyclone 2 toward the United Kingdom.

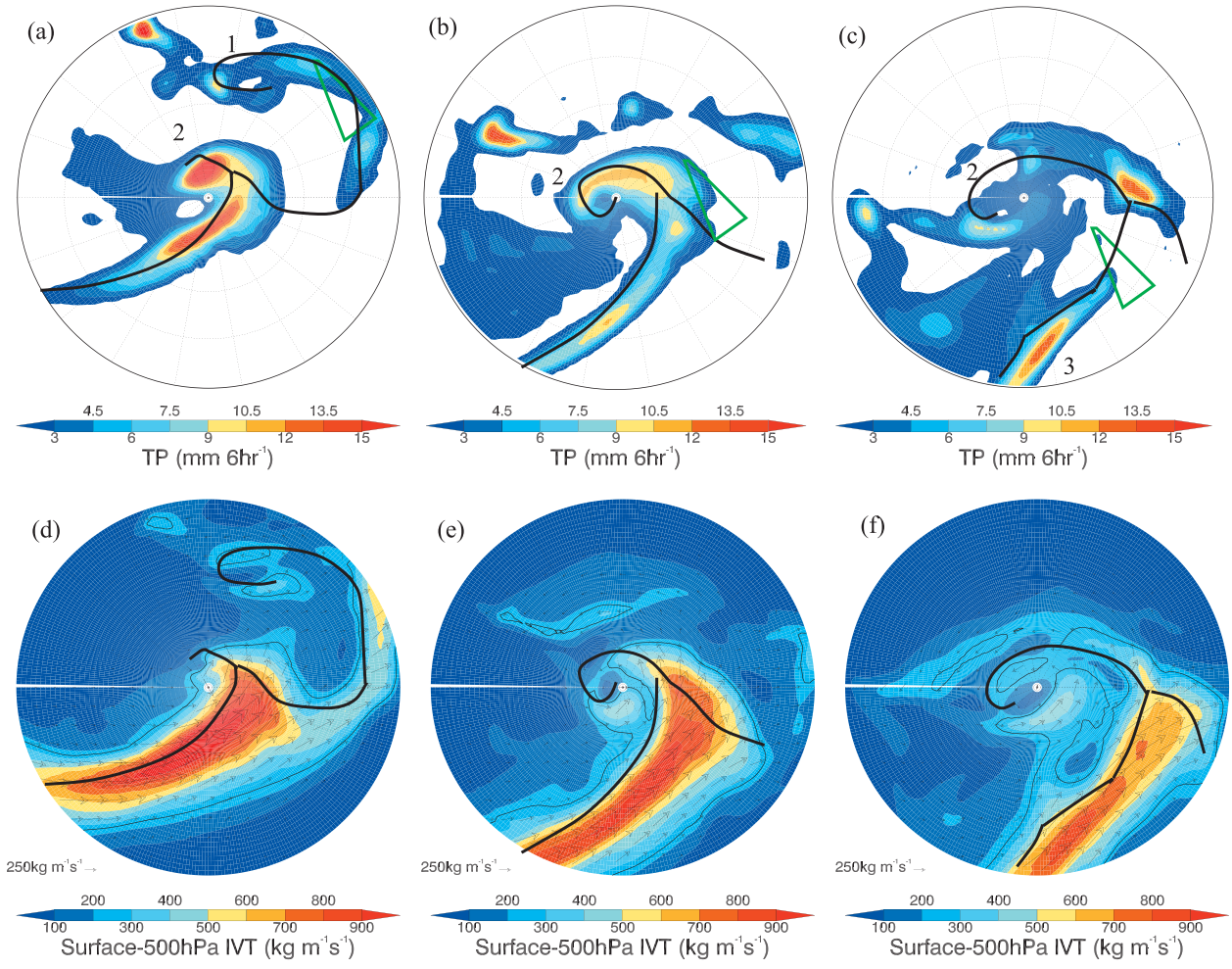

Fig. 3. Time evolution of cyclone-centered fields for (a)–(c) 6-hourly accumulated total precipitation overlaid with frontal positions and (d)–(f) integrated water vapor transport magnitude and vectors, overlaid with IVT = 250 kg m^{-1} s^{-1} (black contour): (a) 24 h before maximum intensity, (b) 12 h before maximum intensity, and (c) at time of max intensity. The green triangle represents the approximate position of the United Kingdom. Labels 1, 2, and 3 represent three successive cyclones.

In this case, therefore, the high TCWV band shown in Fig. 2d is associated with a family of cyclones all traveling along the same path. This results in multiple precipitation events over the United Kingdom; thus, flooding is exacerbated as the precipitation falls over already wet ground (Hand et al. 2004; Ralph et al. 2004, 2013). Furthermore, a secondary cyclone that follows in the footprints of a previous parent cyclone may profit from the high TCWV band created by the parent, leading to more intense precipitation in subsequent cyclones.

Water vapor budget. In this section, we now examine the individual terms in the water vapor budget equation in order to determine the sources of water vapor contributing to precipitation and transport of water vapor.

Figure 4a shows the surface precipitation flux at 0600 UTC 1 February 2002. This is the same figure as Fig. 2c but shown on a different scale with different units. (It is assumed that precipitation is at the same rate for the entire 6-h period.) Figure 4b shows the surface evaporation flux at the same time. There is widespread evaporation from the sea surface within the domain, although the evaporation fluxes are generally small ($<0.2 \times 10^{-3}$ kg m^{-2} s^{-1}). The greatest surface evaporation at this time occurs in the cold sector immediately behind the cold front. Figure 4c shows the negative of the rate of change of water vapor in each column of the domain. As the instantaneous specific humidity is only available every 6 h from ERA-Interim, the rate of change of water vapor in each column is calculated using the instantaneous values 6 h prior to and 6 h after the time of interest. This results in a

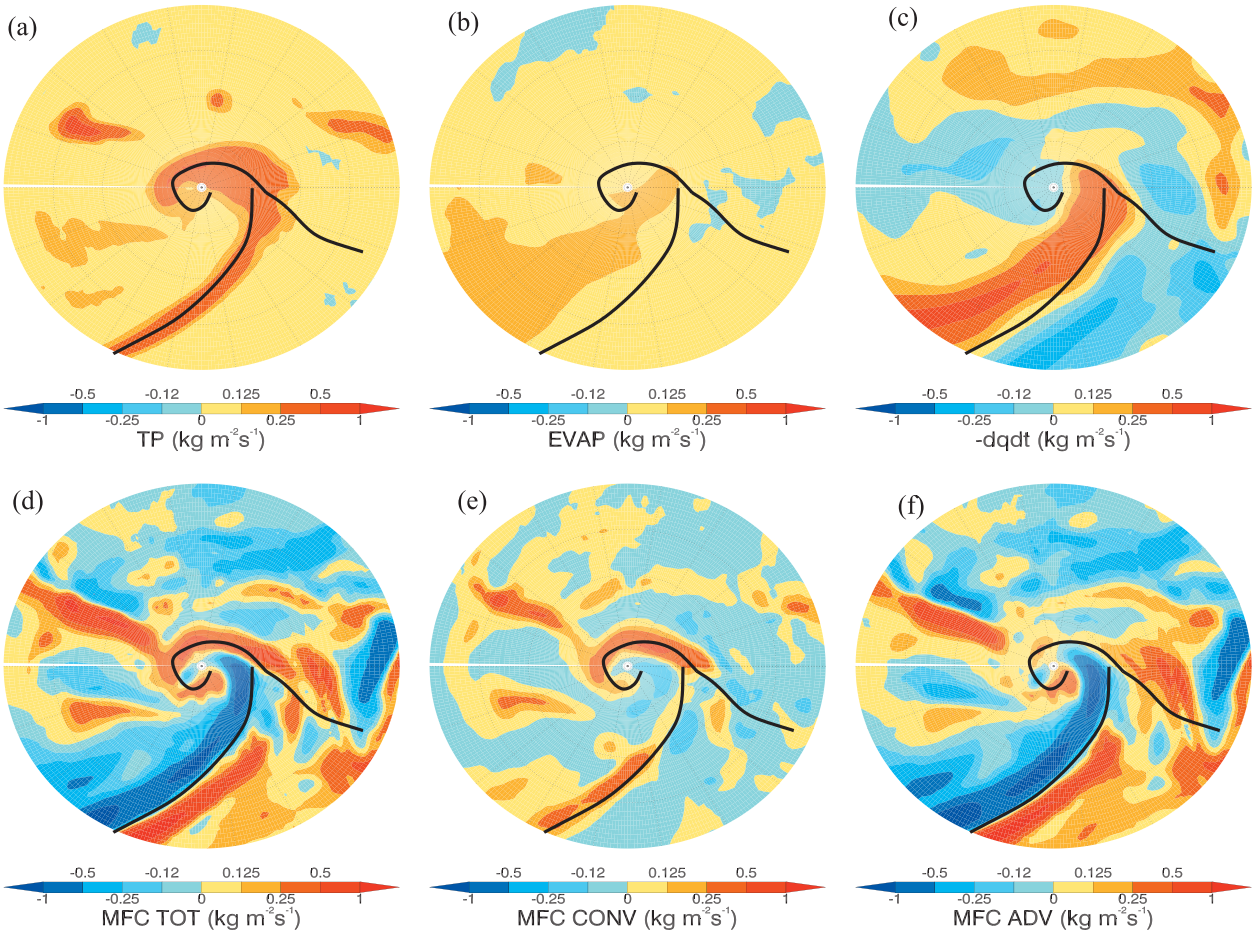

Fig. 4. Cyclone-centered water vapor budget terms at 0600 UTC 1 Feb 2002: (a) precipitation [term 1 in Eq. (1): P], (b) evaporation [term 2 in Eq. (1): E], (c) vertically integrated rate of change of water vapor [term 3 in Eq. (1): $-dq/dt$], (d) vertically integrated total moisture flux convergence [term 1 in Eq. (2): MFC_{TOTAL}], (e) vertically integrated mass convergence [term 2 in Eq. (2): MFC_{CONV}], and (f) vertically integrated advection [term 3 in Eq. (2): MFC_{ADV}]. All figures have units of $\times 10^{-3}$ kg m^{-2} s^{-1} and are overlaid with frontal positions.

smoother field than would be calculated if fields at higher frequency were available. The dominant feature in Fig. 4c is the dipole of positive and negative values on either side of the cold front. This indicates that water vapor content decreases in columns behind the cold front but increases in columns ahead of the cold front in the warm sector.

The moisture flux convergence term can be calculated as a residual time-averaged value [using Eq. (1)] or as an instantaneous value using the instantaneous specific humidity and wind fields. Figure 4d shows the instantaneous moisture flux convergence, calculated using the system-relative wind fields (calculated by subtracting the system propagation speed from the absolute wind fields). Divergence of moisture occurs behind the cold front and convergence of moisture occurs along the frontal boundaries. The instantaneous moisture flux convergence is similar to that calculated using the time-averaged fields but the magnitude of the fluxes is larger. Averaging the instantaneous moisture flux convergence over three time steps (6 h prior to time of interest, time of interest, and 6 h after time of interest) shows that the difference in the magnitudes is due to the partial cancellation of positive and negative fluxes ahead of and behind the cold front as the cold front moves cyclonically (not shown).

We can split the total instantaneous moisture flux convergence into its convergent and advection components. Figure 4e shows the mass convergence term in Eq. (2) calculated using the analyzed fields. As expected, this field bears a close resemblance to the precipitation field in Fig. 4a, despite being an instantaneous field. Mass convergence ahead of the cold front leads to slantwise ascent, condensation of water vapor, and thus precipitation formation. Figure 4f shows the advection term in Eq. (2) calculated using the analyzed fields. Negative

advection of water vapor occurs behind the cold front as the system-relative winds advect relatively dry air behind the cold front cyclonically. Positive advection of water vapor occurs ahead of the cold front as the cold front sweeps high water vapor content into this region. The magnitude and extent of the negative water vapor advection region exceeds that of the positive water vapor advection region. This imbalance results in moisture accumulating along the cold frontal boundary. Thus, the relative motion of the cold front acts to form and maintain the filament of high TCWV values parallel to the cold front as the cyclone moves poleward. Thus, the separation of the total MFC into its convergent and advection components highlights the difference between the formation of the atmospheric river by advection of moisture and the large-scale mass convergence and ascent beneath the cloud head and along the occluded front. The total MFC or IVT cannot distinguish these two processes, which act in different parts of the cyclone.

To further illustrate this point, Fig. 5 shows the moisture flux calculated using the absolute winds and system-relative winds. Although the absolute flow suggests a strong flux of water vapor from outside the cyclone domain toward the cyclone center (Fig. 5a), the system-relative flux of water vapor (Fig. 5b) shows that this is not the case. As the cyclone travels with a speed and direction that is comparable to the wind speed and direction ahead of the cold front, the alongfront component of the system-relative IVT in this region is small and hence the water vapor flux toward the cyclone center is also small. Closer to the cyclone's warm front, the system-relative winds gain an alongfront component before splitting into a cyclonic and anticyclonic branch as the airflow rises up over the warm front (this is identified as the warm conveyor belt airflow; Harrold 1973). Thus, in this region the warm conveyor belt airflow transports water vapor cyclonically into the cloud head and anticyclonically into the cloud shield. The reduced alongfront transport in this Lagrangian framework does not mean that there is no poleward transport of water vapor by the cyclone but that there is little poleward transport of water vapor into the cyclone system itself. Thus, instead of poleward transport occurring because of a direct and continuous feed of moist air from the subtropics to the extratropics (as suggested by the term "atmospheric river"), poleward transport is the result of a continuous cycling of moisture within the cyclone itself. Local convergence of moisture, occurring ahead of the cold front, provides a source of moisture at the base of the warm conveyor belt airflow, which ascends in a slantwise motion, reaches saturation, and forms precipitation. Subsequent convergence of

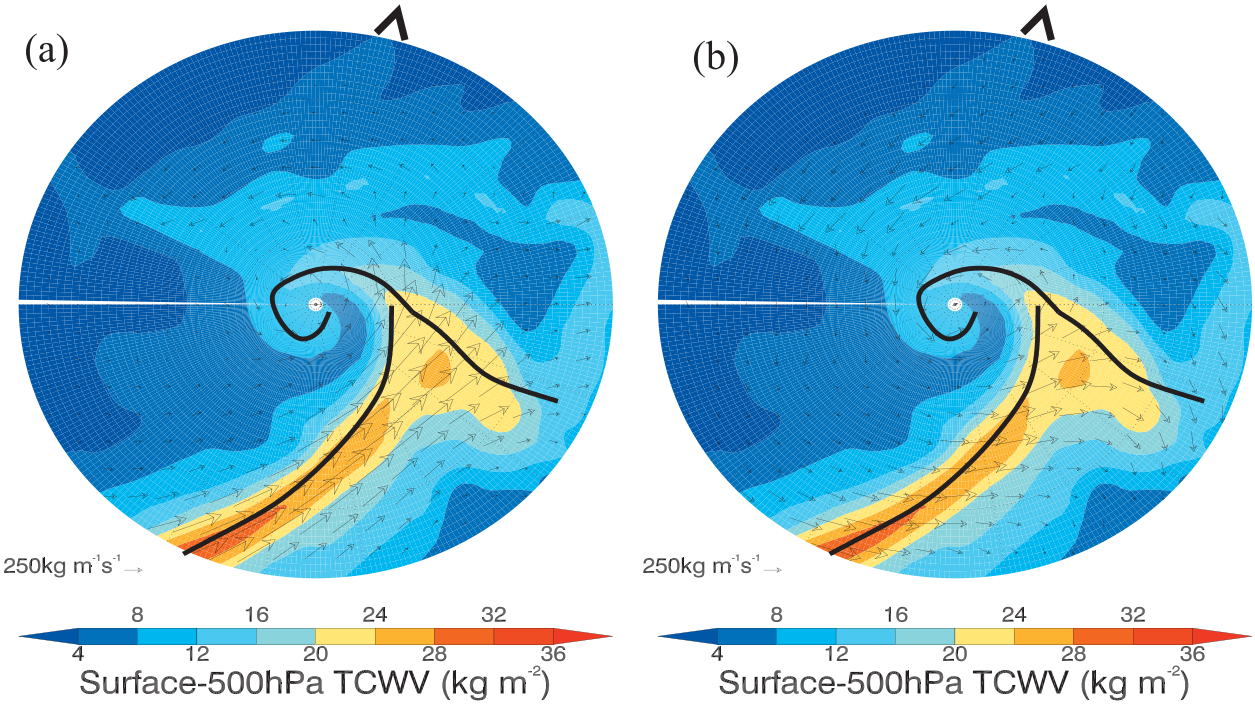

Fig. 5. Cyclone-centered water vapor transport at 0600 UTC 1 Feb 2002. Surface–500-hPa TCWV (kg m^{-2}), as in Fig. 2d, is overlaid with (a) surface–500-hPa moisture flux vectors and (b) surface–500-hPa system-relative moisture flux vectors. Both panels are overlaid with frontal positions. The black arrow head shows the direction of cyclone propagation.

moisture results in a continuous cycle; thus, the saturated air is formed by the cyclone and moves with the cyclone, leaving behind a footprint of where the cyclone has been as the cyclone travels poleward.

Domain-integrated water vapor budgets. Figure 6 shows how the domain-integrated terms in the water vapor budget evolve with time for the cyclone on 1 February 2002. The largest term is the domain-integrated precipitation. The precipitation flux increases during the first 24 h of the cyclone lifetime and peaks 12 h before the time of maximum intensity. After this, the domain-integrated precipitation gradually decreases with time. The next largest term is the domain-integrated evaporation flux. Although the evaporation flux is relatively small at each location, the domain-integrated value contributes significantly to the total water vapor in the atmosphere. The domain-integrated rate of change of water vapor is negative ($-dq/dt > 0$) throughout the cyclone's life cycle, indicating that the water vapor leaving the cyclone domain, via precipitation and divergence, exceeds the water vapor entering the cyclone domain via evaporation and convergence. The domain-integrated system-relative moisture flux convergence is relatively small. For this cyclone, it is small or negative during the cyclone's evolution. As only a small amount of water vapor converges into the domain at the start of the cyclone's evolution, this implies that local sources of water vapor from within the domain dominate the contribution of water vapor available for cyclone precipitation.

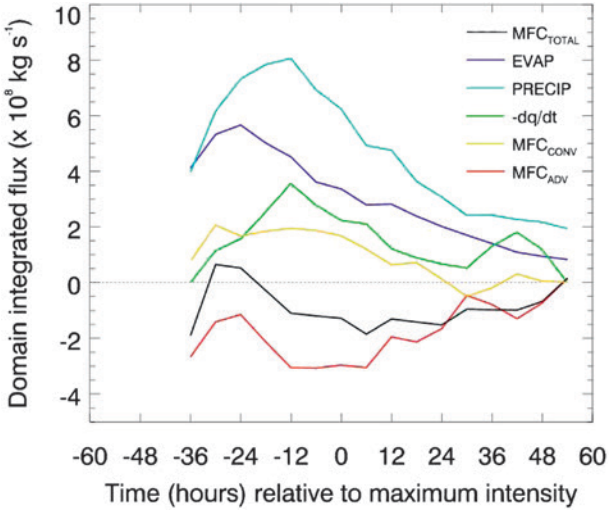

Fig. 6. Time evolution of water vapor budget terms: domain-integrated precipitation (cyan); evaporation (dark blue); rate of change of water vapor (green); total moisture flux convergence MFC_{TOTAL} (black); MFC mass convergence term in Eq. (2), MFC_{CONV} (yellow); and MFC advection term in Eq. (2), MFC_{ADV} (red) for the 1 Feb 2002 storm.

Also shown in Fig. 6 are the terms that contribute to water vapor convergence. As expected, the domain-integrated mass convergence term is positive throughout the majority of the cyclone's evolution. The domain-integrated advection term is negative and largely balances the local mass convergence term. For this cyclone, therefore, external sources of water vapor (>1500 km from cyclone center) contribute a negligible or even negative amount of water vapor available for precipitation formation. The dominant source of water vapor therefore comes from within the domain.

CLIMATOLOGY OF 200 NORTH ATLANTIC CYCLONES. *Climatology: Domain-integrated water vapor budgets*. Figure 7 shows the domain-integrated water vapor budget for a climatology of 200 extratropical cyclones. The individual terms in the budget are smoother than for the individual case study, but their relative importance does not change. As for the case study, domain-integrated precipitation dominates, peaking 12 h before maximum intensity. This is consistent with the results of Bengtsson et al. (2009). Evaporation also peaks 12 h before maximum intensity. The domain-integrated rate of change of water vapor is negative ($-dq/dt > 0$) throughout almost the entire period of the cyclone's life cycle. The resultant moisture flux convergence is again small and slightly positive in the very early stages of development but becoming negative during the period of maximum intensification and decay.

Local horizontal mass convergence is positive throughout the entire cyclone life cycle and is responsible for transporting water vapor into the base of the warm conveyor belt. In a system-relative sense, water vapor is actually exported from the cyclone during the period of maximum intensification (36–0 h prior to maximum intensity) and during its decaying phase. Thus, the cyclone effectively leaves a footprint of high water vapor content air behind it as it travels poleward.

As a fraction of the total precipitation, external moisture flux convergence contributes a negligible or even negative amount to the vapor available for precipitation formation. These results are consistent with the results of Sodemann and Stohl (2013), who showed that during intense precipitation events in Norway <20% of the water vapor originated south of 50°N. Similarly, Knippertz and Wernli (2010), in a 23-year climatology of tropical moisture export, found that the contribution of tropical moisture to precipitation in the extratropical Atlantic was also below 20%.

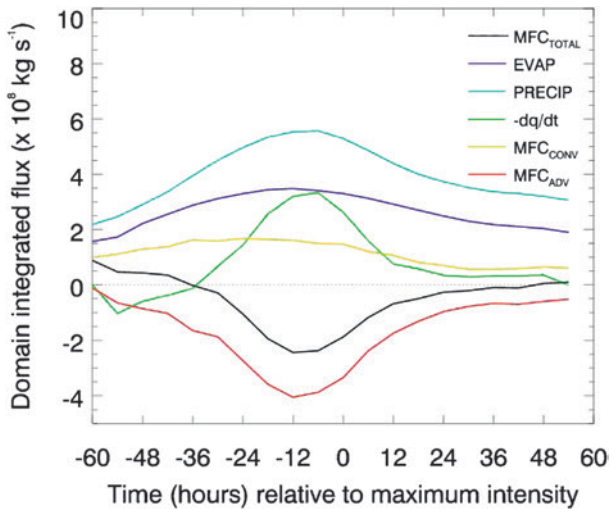

Fig. 7. As in Fig. 6, but for composite of 200 wintertime North Atlantic cyclones.

DISCUSSION AND CONCLUSIONS. In this paper, we investigate the spatial distribution and transport of water vapor within a climatology of extratropical cyclones. The 200 most intense extratropical cyclones are identified and tracked in the ERA-Interim 1979–2009 reanalysis using 850-hPa relative vorticity. The individual terms in the water vapor budget equation are calculated for each of the 200 cyclones. Evaporation of water vapor from the sea surface, occurring mostly behind the cold front, contributes significantly to the total cyclone water vapor throughout the entire cyclone life cycle. The total cyclone-integrated water vapor decreases throughout its life cycle as the water vapor lost from the atmosphere by precipitation exceeds that gained via evaporation or water vapor convergence.

Water vapor convergence into and out of the system is negligible and even negative during the most rapidly intensifying stage of the cyclone evolution showing that water vapor is actually exported from the system leaving a water vapor footprint behind the cyclone as it travels poleward. To further investigate this, the local mass convergence and advection of water vapor flux terms are calculated. It is shown that, as the cold front moves cyclonically toward the warm front, causing the warm sector to narrow, local convergence of water vapor occurs along the cold front and is thus responsible for creating the band of high TCWV.

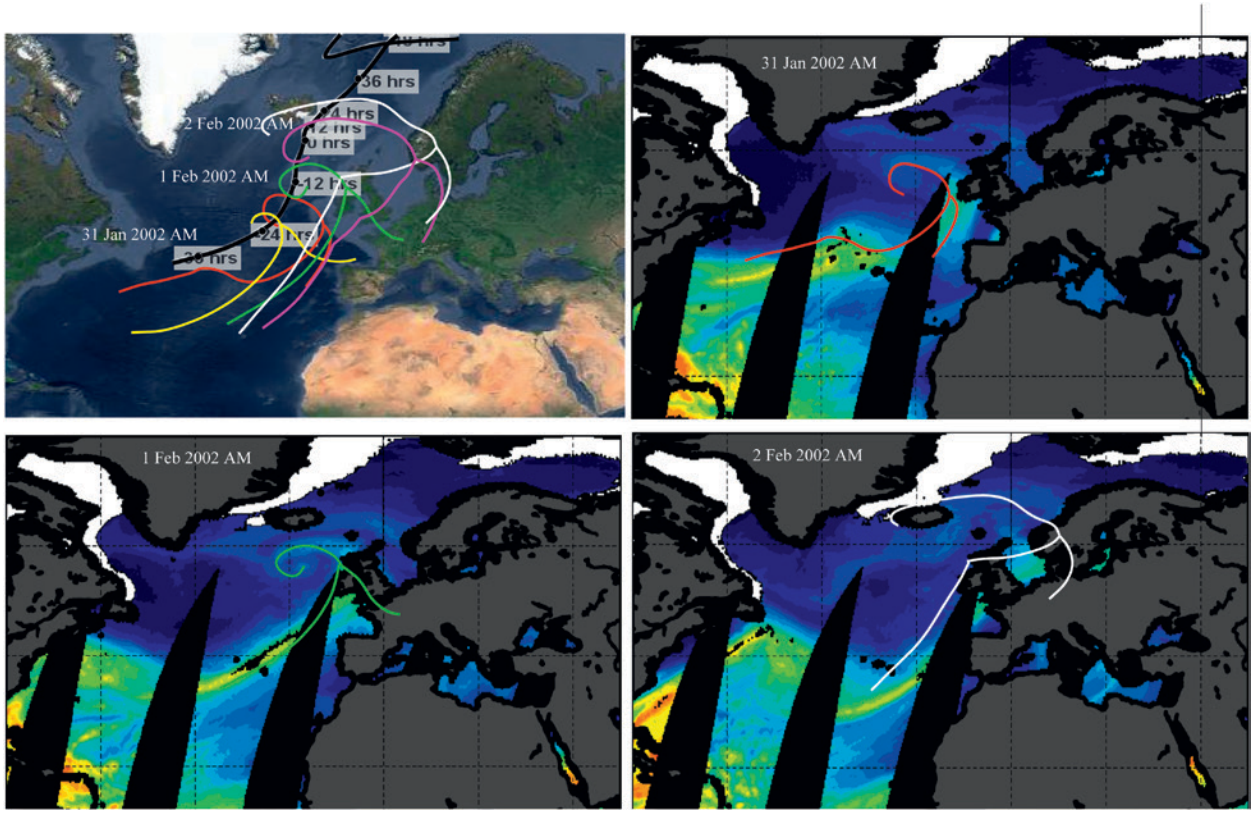

Fig. 8. (a) Schematic showing positions of surface fronts at successive 12-hourly intervals, starting at 0600 UTC 31 Jan 2002. (b) SSM/I (F13)-integrated water vapor on 31 Jan 2002 overlaid with 0600 UTC 31 Jan 2002 frontal positions. (c) SSM/I on 1 Feb 2002 overlaid with 0600 UTC 1 Feb 2002 frontal positions. (d) SSM/I on 2 Feb 2002 overlaid with 0600 UTC 2 Feb 2002 frontal positions.

Figure 8 is a schematic showing the relative positions of surface fronts and regions of high TCWV for the case study cyclone on 1 February 2002. The band of high integrated water vapor narrows as the cold front moves cyclonically toward the warm front, sweeping up water vapor as it travels. The location of the band of high water vapor travels farther from the cyclone center as the cyclone evolves because of the process of frontal fracturing. By the decaying stage of the cyclone evolution the band is >1000 km from the cyclone center. The filaments of high water vapor content seen in the Special Sensor Microwave Imager (SSM/I) satellite imagery represent the footprints left behind as the cyclone channels atmospheric moisture into a narrow band as it travel poleward from its origin in the subtropics.

This paper supports the conclusions reached in idealized and Lagrangian studies that local sources of water vapor are responsible for the formation and maintenance of bands of high TCWV found ahead of the cold front in the cyclone's warm sector. Furthermore, it suggests that the filamentary structures of high TCWV are the result of water vapor export, resulting in footprints left behind as cyclones travel poleward.

ACKNOWLEDGMENTS. We are grateful to Kevin Hodges at the National Centre for Earth Observation, Reading, for supplying us with his tracking algorithm. We appreciate the useful discussions on this work provided by Matt Hawcroft (University of Reading) and Jun-Ichi Yano (Météo-France).

REFERENCES

Bader, M. J., and W. T. Roach, 1977: Orographic rainfall in warm sectors of depressions. *Quart. J. Roy. Meteor. Soc.,* **103,** 269–280, doi:10.1002/qj.49710343605.

Bao, J. W., S. A. Michelson, P. J. Neiman, F. M. Ralph, and J. M. Wilczak, 2006: Interpretation of enhanced integrated water vapor bands associated with extratropical cyclones: Their formation and connection to tropical moisture. *Mon. Wea. Rev.,* **134,** 1063–1080, doi:10.1175/MWR3123.1.

Bengtsson, L., K. I. Hodges, and N. Keenlyside, 2009: Will extratropical storms intensify in a warmer climate? *J. Climate,* **22,** 2276–2301, doi:10.1175/2008JCLI2678.1.

Boutle, I. A., R. J. Beare, S. E. Belcher, A. R. Brown, and R. S. Plant, 2010: The moist boundary layer under a mid-latitude weather system. *Bound.-Layer Meteor.,* **134,** 367–386, doi:10.1007/s10546-009-9452-9.

——, S. E. Belcher, and R. S. Plant, 2011: Moisture transport in midlatitude cyclones. *Quart. J. Roy. Meteor. Soc.,* **137,** 360–373, doi:10.1002/qj.783.

Browning, K. A., 1990: Rain, rainclouds and climate. *Quart. J. Roy. Meteor. Soc.,* **116,** 1025–1051, doi:10.1002/qj.49711649502.

Catto, J. L., L. C. Shaffrey, and K. I. Hodges, 2010: Can climate models capture the structure of extratropical cyclones? *J. Climate,* **23,** 1621–1635, doi:10.1175/2009JCLI3318.1.

Cordeira, J. M., F. M. Ralph, and B. J. Moore, 2013: The development and evolution of two atmospheric rivers in proximity to western North Pacific tropical cyclones in October 2010. *Mon. Wea. Rev.,* **141,** 4234–4255, doi:10.1175/MWR-D-13-00019.1.

Dacre, H. F., and S. L. Gray, 2009: The spatial distribution and evolution characteristics of North Atlantic cyclones. *Mon. Wea. Rev.,* **137,** 99–115, doi:10.1175/2008MWR2491.1.

——, and ——, 2013: Quantifying the climatological relationship between extratropical cyclone intensity and atmospheric precursors. *Geophys. Res. Lett.,* **40,** 2322–2327, doi:10.1002/grl.50105.

——, M. K. Hawcroft, M. A. Stringer, and K. I. Hodges, 2012: An extratropical cyclone database: A tool for illustrating cyclone structure and evolution characteristics. *Bull. Amer. Meteor. Soc.,* **93,** 1497–1502, doi:10.1175/BAMS-D-11-00164.1.

Dee, D. P., and Coauthors, 2011: The ERA-Interim reanalysis: Configuration and performance of the data assimilation system. *Quart. J. Roy. Meteor. Soc.,* **137,** 553–597, doi:10.1002/qj.828.

de Leeuw, J., J. Methven, and M. Blackburn, 2015: Evaluation of ERA-Interim reanalysis precipitation products using England and Wales observations. *Quart. J. Roy. Meteor. Soc.,* **141,** 798–806 doi:10.1002/qj.2395.

Dettinger, M., 2013: Atmospheric rivers as drought busters on the U.S. West Coast. *J. Hydrometeor.,* **14,** 1721–1732, doi:10.1175/JHM-D-13-02.1.

Gray, S. L., and H. F. Dacre, 2006: Classifying dynamical forcing mechanisms using a climatology of extratropical cyclones. *Quart. J. Roy. Meteor. Soc.,* **132,** 1119–1137, doi:10.1256/qj.05.69.

Guan, B., N. P. Molotch, and D. E. Waliser, 2013: The 2010/2011 snow season in California's Sierra Nevada: Role of atmospheric rivers and modes of large-scale variability. *Water Resour. Res.,* **49,** 6731–6743, doi:10.1002/wrcr.20537.

Hand, W. H., N. I. Fox, and C. G. Collier, 2004: A study of twentieth century extreme rainfall events in the United Kingdom with implications for forecasting. *Meteor. Appl.,* **11,** 15–31, doi:10.1017/S1350482703001117.

Harrold, T. W., 1973: Mechanisms influencing the distribution of precipitation within baroclinic disturbances. *Quart. J. Roy. Meteor. Soc.,* **99,** 232–251, doi:10.1002/qj.49709942003.

Hawcroft, M. K., L. C. Shaffrey, K. I. Hodges, and H. F. Dacre, 2012: How much Northern Hemisphere precipitation is associated with extratropical cyclones? *Geophys. Res. Lett.,* **39,** L24809, doi:10.1029/2012GL053866.

Hill, F. F., K. A. Browning, and M. J. Bader, 1981: Radar and raingauge observations of orographic rain over south Wales. *Quart. J. Roy. Meteor. Soc.,* **107,** 643–670, doi:10.1002/qj.49710745312.

Hodges, K. I., 1995: Feature tracking on the unit sphere. *Mon. Wea. Rev.,* **123,** 3458–3465, doi:10.1175/1520-0493(1995)123<3458:FTOTUS>2.0.CO;2.

Kim, J., D. E. Waliser, and P. J. Neiman, 2013: Effects of atmospheric river landfalls on the cold season precipitation in California. *Climate Dyn.,* **40,** 465–474, doi:10.1007/s00382-012-1322-3.

Knippertz, P., and J. E. Martin, 2007: A Pacific moisture conveyor belt and its relationship to a significant precipitation event in the semiarid southwestern United States. *Wea. Forecasting,* **22,** 125–144, doi:10.1175/WAF963.1.

——, and H. Wernli, 2010: A Lagrangian climatology of tropical moisture exports to the Northern Hemispheric extratropics. *J. Climate,* **23,** 987–1003, doi:10.1175/2009JCLI3333.1.

Lackmann, G. M., and J. R. Gyakum, 1999: Heavy cold-season precipitation in the northwestern United States: Synoptic climatology and an analysis of the flood of 17–18 January 1986. *Wea. Forecasting,* **14,** 687–700, doi:10.1175/1520-0434(1999)014<0687:HCSPIT>2.0.CO;2.

Lavers, D. A., R. P. Allan, E. F. Wood, G. Villarini, D. J. Brayshaw, and A. J. Wade, 2011: Winter floods in Britain are connected to atmospheric rivers. *Geophys. Res. Lett.,* **38,** L23803, doi:10.1029/2011GL049783.

——, G. Villarini, R. P. Allan, E. F. Wood, and A. J. Wade, 2012: The detection of atmospheric rivers in atmospheric reanalyses and their links to British winter floods and the large-scale climatic circulation. *J. Geophys. Res.,* **117,** D20106, doi:10.1029/2012JD018027.

Matrosov, S. Y., 2013: Characteristics of landfalling atmospheric rivers inferred from satellite observations over the eastern North Pacific Ocean. *Mon. Wea. Rev.,* **141,** 3757–3768, doi:10.1175/MWR-D-12-00324.1.

Moore, B. J., P. J. Neiman, F. M. Ralph, and F. E. Barthold, 2012: Physical processes associated with heavy flooding rainfall in Nashville, Tennessee, and vicinity during 1–2 May 2010: The role of an atmospheric river and mesoscale convective systems. *Mon. Wea. Rev.,* **140,** 358–378, doi:10.1175/MWR-D-11-00126.1.

Neiman, P. J., F. M. Ralph, G. A. Wick, J. D. Lundquist, and M. D. Dettinger, 2008: Meteorological characteristics and overland precipitation impacts of atmospheric rivers affecting the west coast of North America based on eight years of SSM/I satellite observations. *J. Hydrometeor.,* **9,** 22–47, doi:10.1175/2007JHM855.1.

——, L. J. Schick, F. M. Ralph, M. Hughes, and G. A. Wick, 2011: Flooding in western Washington: The connection to atmospheric rivers. *J. Hydrometeor.,* **12,** 1337–1358, doi:10.1175/2011JHM1358.1.

——, M. Hughes, and B. J. Moore, 2013: Sierra barrier jets, atmospheric rivers, and precipitation characteristics in Northern California: A composite perspective based on a network of wind profilers. *Mon. Wea. Rev.,* **141,** 4211–4233, doi:10.1175/MWR-D-13-00112.1.

Ralph, F. M., P. J. Neiman, and G. A. Wick, 2004: Satellite and CALJET aircraft observations of atmospheric rivers over the eastern North Pacific Ocean during the winter of 1997/98. *Mon. Wea. Rev.,* **132,** 1721–1745, doi:10.1175/1520-0493(2004)132<1721:SACAOO>2.0.CO;2.

——, T. Coleman, P. J. Neiman, R. J. Zamora, and M. D. Dettinger, 2013: Observed impacts of duration and seasonality of atmospheric-river landfalls on soil moisture and runoff in coastal Northern California. *J. Hydrometeor.,* **14,** 443–459, doi:10.1175/JHM-D-12-076.1.

Rivera, E. R., F. Dominguez, and C. L. Castro, 2014: Atmospheric rivers and cool season extreme precipitation events in the Verde River basin of Arizona. *J. Hydrometeor.,* **15,** 813–829, doi:10.1175/JHM-D-12-0189.1.

Rutz, J. J., W. J. Steenburgh, and F. M. Ralph, 2014: Climatological characteristics of atmospheric rivers and their inland penetration over the western United States. *Mon. Wea. Rev.,* **142,** 905–921, doi:10.1175/MWR-D-13-00168.1.

Simmons, A. J., K. M. Willett, P. D. Jones, P. W. Thorne, and D. P. Dee, 2010: Low-frequency variations in surface atmospheric humidity, temperature, and precipitation: Inferences from reanalyses and monthly gridded observational data sets. *J. Geophys. Res.,* **115,** D01110, doi:10.1029/2009JD012442.

Smith, B. L., S. E. Yuter, P. J. Neiman, and D. E. Kingsmill, 2010: Water vapor fluxes and orographic precipitation over Northern California associated with a landfalling atmospheric river. *Mon. Wea. Rev.,* **138,** 74–100, doi:10.1175/2009MWR2939.1.

Sodemann, H., and A. Stohl, 2013: Moisture origin and meridional transport in atmospheric rivers and their association with multiple cyclones. *Mon. Wea. Rev.,* **141,** 2850–2868, doi:10.1175/MWR-D-12-00256.1.

Viale, M., and M. N. Nunez, 2011: Climatology of winter orographic precipitation over the subtropical

central Andes and associated synoptic and regional characteristics. *J. Hydrometeor.,* **12,** 481–507, doi:10.1175/2010JHM1284.1.

Wick, G. A., P. J. Neiman, and F. M. Ralph, 2013: Evaluation of forecasts of the water vapor signature of atmospheric rivers in operational numerical weather prediction models. *Wea. Forecasting,* **28,** 1337–1352, doi:10.1175/WAF-D-13-00025.1.

Zhu, Y., and R. E. Newell, 1998: A proposed algorithm for moisture fluxes from atmospheric rivers. *Mon. Wea. Rev.,* **126,** 725–735, doi:10.1175/1520-0493(1998)126<0725:APAFMF>2.0.CO;2.

AMS titles now available as eBooks at springer.com

AMS BOOKS

RESEARCH | APPLICATIONS | HISTORY

www.ametsoc.org/amsbookstore

Springer

Scan to see AMS eBook titles at springer.com

AMERICAN METEOROLOGICAL SOCIETY